G-phase strengthened iron alloys by design

D. J. M. King[a,*], Mujin Yang[b], T. M. Whiting[a], Xingjun Liu[b, c] M. R. Wenman[a]

[a] *Centre for Nuclear Engineering, Imperial College London, South Kensington, London, SW7 2AZ, United Kingdom*
[b] *Institute of Materials Genome and Big Data, Harbin Institute of Tehnology, Shenzhen 518055, PR China*
[c] *State Key Laboratory of Advanced Welding and Joining, Harbin Institute of Technology, Harbin 150001, PR China*

**Corresponding Author:*
E-mail: daniel.miks@live.com

Abstract. Density functional theory (DFT) calculations were used to model G-phase precipitates of formula $X_6M_{16}Si_7$ where X is Cr, Hf, Mn, Mo, Nb, Ta, Ti, V, W and Zr and M is either Fe or Ni. It was found that the occupancy of the d-orbital is correlated to the formation enthalpies of each structure. Past thermal expansion coefficient data was used to predict the lattice misfit between each G-phase and body centred cubic (BCC) Fe. All except Hf and Zr containing G-phases were predicted to have zero misfit between 581−843 K. Of the Ni containing G-phases, $Mn_6Ni_{16}Si_7$ was predicted to have the most similar elastic properties to BCC Fe. DFT calculations of the substitution energies of Al, Cr Cu, Fe, Ge, Hf, Mo, Nb, P, Ta, Ti, V, Zr, and vacancies onto the $Mn_6Ni_{16}Si_7$ G-phase from BCC Fe were performed. It was predicted that Cu, P and vacancies favour G-phase substitution. Suppression of the G-phase is predicted when Si content is reduced by half, at which point the BCC phase is favoured. It is hypothesised that including Zr to form a $(Mn,Zr)_6Ni_{16}Si_7$ precipitate will allow for higher ageing temperature and expediate nucleation in an Fe alloy. Thermocalc was used to predict that a mixture of $Fe_{bal}Cr_9Ni_4Si_2(Mn_{0.6}Zr_{0.4})_{1.2}$ (at.%) will produce a G-phase strengthened Fe alloy with potential for a good balance of strength, ductility and oxidation/corrosion resistance at room temperature. This alloy composition was experimentally determined to precipitate the G-phase in ≤24 h with cube-on-cube orientation to the BCC Fe matrix.

Keywords: G-phase; solute clustering; density functional theory; duplex steels; ferritic

1. Introduction

A mechanistic understanding of the G-phase in steels/iron alloys is of interest to oil, chemical and nuclear industries [1–3]. This is because it forms in both thermally aged stainless and ferritic steels, and is thought to compromise structural integrity during long term operation in elevated temperature environments (573-1100 K). Stoichiometric G-phase exists as $X_6M_{16}Z_7$ in a $Fm\bar{3}m$, $D8_a$ (ordered Th_6Mn_{23}) structure [4] where X = Gr IV-VII transition metals, M = Fe, Co, Ni, and Z = As, P, Si have been experimentally observed. In steels, the G-phase was first observed to precipitate at grain boundaries (giving rise to its designation as "grain boundary phase" [5]), however, it has subsequently been observed to form in the matrix of the α-Fe, on dislocations, and α/γ, α/α' phase boundaries [6,7]. A considerable amount of work has been done, that is still ongoing in the nuclear industry, to understand and prevent the solute clustering of Mn, Ni and Si (thought to be a precursor to the $Mn_6Ni_{16}Si_7$ G-phase in low-alloy ferritic steels [8,9]), which is potentially a limiting factor for the lifetime of pressurised water reactors [10]. Conversely, recent work to promote G-phase formation to achieve higher room temperature yield strengths (1700 MPa) in ferritic steels is gaining popularity [11–13]. It is theorised that precipitates with coherent phase boundaries with low lattice misfit to the surrounding ferrite matrix

(as can occur with the G-phase in steels) is a desirable trait for high strengths to be achieved while maintaining ductility [14].

Off-stoichiometric G-phase is commonly observed and its accommodation of various other species has been evidenced by chemical analysis techniques [15]. The effect of these elements are of great importance to the predictability and control of G-phase formation; however, little work has been done to characterise their influence on stability and lattice mismatch.

In this study, density functional theory (DFT) was used to calculate formation energies, lattice parameters and elastic constants for 22 different G-phase chemistries. The site preferences for substitution of Al, Cr Cu, Fe, Ge, Hf, Mo, Nb, P, Ta, Ti, V, Zr, and a vacancy into the $Mn_6Ni_{16}Si_7$ G-phase were also calculated. The off-stoichiometric G-phase $Fe_{x+y+z}Mn_{6-x}Ni_{16-y}Si_{7-z}$ was examined and compared to BCC structures with the same composition. Thermocalc was used, guided by lessons learned from DFT, to predict compositions that could form dual phase BCC+G-phase microstructures in Fe alloys. One predicted composition [$Fe_{bal}Cr_9Ni_4Si_2(Mn_{0.6}Zr_{0.4})_{1.2}$] at.% and two comparison compositions ($Fe_{bal}Ni_7Si_3Mn_1$ and $Fe_{bal}Ni_3Si_3Mn_1$ at.%) were experimentally produced, aged and characterised to compare with theoretical predictions.

2. Methodology

2.1 Theoretical

A plane-wave density functional theory method was used, as implemented in the Vienna Ab initio Simulation Package (VASP) [16]. Projector augmented wave (PAW) pseudopotentials [17], were used for each element. Semi-core *s* states were considered valence electrons for Zr (12), semi-core *p* states were considered valence electrons for Co (15), Cr (12), Cu (17), Fe (14), Hf (10), Mn (13), Mo (12), Nb (11) Ni (16), Ta (11), Ti (10), V (11), W (6) and a standard number of electrons for Al (3), C (4), Ge (4), P (5) and Si (4).

The *k*-points, cut-off energy and lattice parameters of the pure elements in their ground state structures were converged independently. It was determined that a real space *k*-point density of 0.02 $Å^{-3}$ and a cut-off energy of 500 eV would provide accurate results, within 10^{-3} eV, and were kept consistent to calculate formation enthalpies and lattice parameters in all alloyed structures. The Methfessel Paxton [18] smearing method (width 0.1 eV) was used and full geometry relaxations were carried out under constant pressure for all reference structures. Collinear spin polarisation effects were included. For the exchange-correlation functional, the generalised gradient approximation as developed by Perdew-Burke-Ernzerho [19] (GGA-PBE) was utilised. The convergence criterion for electronic convergence was 10^{-6} eV and for geometry optimisation was 10^{-4} eV.

For the calculations of the density of states (DOS) and elastic constants the cut-off energy was increased to 650 eV and k-point density decreased 0.01 $Å^{-3}$. The tetrahedron smearing method with Blöchl corrections [20] were used for constant volume calculations to generate the electronic density of states. The elastic constants were assessed using the stress-strain method [21] implemented within VASP. Six finite distortions were imposed, and each atom was displaced twice by 0.01 Å (accounting for symmetry) in both the ±x, ±y and ±z directions in the 29 atom rhombohedral G-phase unit cell (totalling 52 calculations on each composition), to obtain the contributions to the elastic constants by the ionic relaxations. The polycrystalline elastic moduli: shear modulus (*G*), bulk modulus (*B*), Young's modulus (*E*) and Poisson's ratio (*v*) were then calculated using the Hill's approach with Voigt's and Reuss's approximations [22].

To calculate the substitution energies of the elements into the $Mn_6Ni_{16}Si_7$ G-phase its stoichiometric, 116 atom, cubic structure was energy minimised and used as a reference structure. Fixed volume and dimension calculations were then performed with a single substitution of the impurity element on the Wycoff sites 4a (Si), 24d (Si), 32f (Ni) and 24e (Mn). Using Cu onto the Mn site as an example, the substitution energies were calculated according to the following reaction:

$$(Cu_1Fe_{127})_{BCC} + (Mn_{24}Ni_{64}Si_{28})_{G\text{-}phase} \rightarrow (Mn_1Fe_{127})_{BCC} + [(Cu_{0.04}Mn_{0.96})_{24}Ni_{64}Si_{28}]_{G\text{-}phase} \quad (1)$$

To simulate concentrated Fe substitution $(Fe_{0.58}Mn_{0.42})_6Ni_{16}Si_7$, $Mn_6(Fe_{0.22}Ni_{0.78})_{16}Si_7$ and $Mn_6Ni_{16}(Fe_{0.5}Si_{0.5})_7$ G-phase (116 atoms) and BCC structures (128 atoms) were simulated at constant pressure. The site occupancies of the BCC supercell were kept consistent with the G-phase i.e. one

sublattice was occupied by Ni and the other by Mn and Si as done in a previous study [23]. The occupancies of Fe were selected pseudo-randomly using a random number generator. The randomisations were performed to produce ten unique supercells of each G-phase and BCC structures. This method has been demonstrated in previous studies [24–26]. For further methodology details can be found in reference [27].

The lattice misfit parameter, δ, was calculated by the equation:

$$\boldsymbol{\delta} = \frac{\mathbf{2}(\boldsymbol{a_{G-phase}} - \boldsymbol{a_{Fe}})}{(\boldsymbol{a_{G-phase}} + \boldsymbol{a_{Fe}})} \quad (2)$$

where $a_{G\text{-}phase}$ and a_{Fe} are the lattice parameters of the G-phase and Fe (taken to be 4×2.83 Å of pure BCC Fe from DFT in this study), respectively.

CALculation of PHase Diagrams (CALPHAD) as implemented within Thermocalc was used to calculate the equilibrium property diagrams of Fe-Cr-Ni-Si-Mn-Zr alloys. The "TCFE7" database was used.

2.2 Experimental

Three alloy ingots were prepared by arc-melting using commercially-pure metals (99.99% in purity), and then drop cast into a copper mould. The following compositions were chosen: $Fe_{bal}Cr_9N_4iSi_2(Mn_{0.6}Zr_{0.4})_{1.1}$, $Fe_{bal}Cr_{20}N_3iSi_3Mn_1$, and $Fe_{bal}N_7iSi_2Mn_1$, where the foremost composition was predicted from the theoretical component of this study, and the latter two were chosen to remove the influence of Cr and Zr and compare to a previous study by Yang *et al.* [28], respectively. Their nominal compositions are shown in table 1. These cast ingots were homogenised at 1525 K for 30 min in evacuated quartz tubes, quenched into ice water and then cut into small pieces for further ageing heat treatment at 773 K for 1-24 h in air, and air-cooled on a ceramic block.

Table 1. Nominal compositions of alloys experimentally investigated within this study (wt.%).

Formula	Fe	Cr	Ni	Mn	Si	Zr
$Fe_{bal}Cr_9N_4iSi_2(Mn_{0.6}Zr_{0.4})_{1.1}$	81.4	9.0	4.0	0.7	2.0	0.4
$Fe_{bal}Cr_{20}N_3iSi_3Mn_1$	73.0	20.0	3.0	1.0	3.0	0.0
$Fe_{bal}N_7iSi_2Mn_1$	90.0	0.0	7.0	1.0	2.0	0.0

A series of aged specimens were then inlaid, polished and tested in a Shimadzu micro-hardness tester under a 4.9 N load and 15 s holding time. Each specimen was tested six times and average values of the measured data were taken. The 24 h aged samples were further analysed in a JEM-2100 (HC) transmission electron microscope (TEM) operating at 200 kV. TEM specimens were initially ground to a thickness of ~50 μm and were then electro-polished at room temperatures and at 28 V using jet-polish techniques in an electrolyte containing 6% $HClO_4$, 12% CH_3COOH and 12% ethylene glycol in methanol.

3. Results and Discussion

3.1 Comparison of G-phase compositions

The formation enthalpies of the various Ni containing G-phase compositions previously observed, or hypothesised to form, were calculated and compared to past literature, see table 2. The lattice parameters of the simulated structures are in good agreement with past experimental findings. Discrepancies are attributed to the approximation of the exchange-correlation functional [29,30] and omission of thermal effects i.e. lattice parameters are calculated at 0 K in the current study and often measured at room temperature experimentally. $Mn_6Ni_{16}Si_7$ has a relatively unfavourable (-12.39 eV/formula unit) formation enthalpy compared to the other combinations. Refractory elements Hf, Zr together with Ti were found to be the most thermodynamically favourable G-phase compositions to form in the $X_6Ni_{16}Si_7$ ternary systems, all with enthalpies less than -20 eV/formula unit, in agreement with past findings [28].

Table 2. Lattice parameter and formation enthalpies of various G-phase precipitates with Ni. The lattice misfit between 4 times the pure Fe α-BCC lattice and respective G-phase denoted as δ.

Composition	Lattice parameter (Å)		δ (%)	$T_{\delta=0\%}$ (K)	Formation enthalpy (eV/formula unit)	
	Literature	Current study			Literature[a]	Current study
$Cr_6Ni_{16}Si_7$	11.10[b]	11.10	-1.96	757	-9.78	-9.35
$Hf_6Ni_{16}Si_7$	11.39[b], 11.41[c]	11.40	0.70	-	-22.58	-22.63
$Mn_6Ni_{16}P_7$	11.03[d]	10.96	-3.23	843	-	-13.36
$Mn_6Ni_{16}Si_7$	**11.15[e], 11.17[f]**	**11.10**	-1.33	**757**	**-12.50**	**-12.39**
$Mo_6Ni_{16}Si_7$	-	11.14	-1.60	716	-12.41	-12.27
$Nb_6Ni_{16}Si_7$	11.24[g]	11.26	-0.53	581	-17.56	-17.23
$Ta_6Ni_{16}Si_7$	11.22[g]	11.23	-0.80	621	-17.60	-17.54
$Ti_6Ni_{16}Si_7$	11.26[g, c]	11.17	-1.33	585	-20.51	-20.49
$V_6Ni_{16}Si_7$	11.13[d]	11.07	-2.27	784	-13.65	-13.59
$W_6Ni_{16}Si_7$	-	11.13	-1.66	728	-10.68	-10.88
$Zr_6Ni_{16}Si_7$	11.47[d]	11.46	1.23	-	-22.57	-22.52

Theoretical: [a]Yang *et al.* [28], Experimental: [b]Glady *et al.* [31], [c]Grystiv *et al.* [32] [d]Chaudout *et al.* [33], [e]Kuz'ma *et al.* [34] [f]Yan *et al.* [4], [g]Holman *et al.* [35]

Recently, it has been proposed that a smaller magnitude of lattice misfit [δ, (Eq. 2)] , of a coherent precipitate to the surrounding matrix, leads to a lower nucleation energy barrier for precipitation and maintenance of ductility after precipitation hardening [14]. It is recognised that the G-phase precipitate has a face centred cubic (FCC) superstructure and may not permit dislocation movement from the matrix through the precipitate. However, it is plausible that the lattice misfit argument holds true for this case, due to the similarities between a 4×4×4 BCC structure and the cubic G-phase i.e. 60 of 116 G-phase lattice sites are shared with the BCC structure and the remaining 56 atoms are only reconstructed slightly from the original positions by ≤0.1052 nm [3,23]. Therefore we continue our analysis assuming that dislocations can move from the matrix through the precipitate and δ could influence the ductility of the alloy. It follows that the $Nb_6Ni_{16}Si_7$ and $Hf_6Ni_{16}Si_7$ precipitates are predicted to have the lowest misfits with a surrounding BCC Fe matrix at 0 K. The misfit predicted for $Mn_6Ni_{16}Si_7$ was within the range recorded in duplex steels (-5.13% [36] to 0.00% [3]). This large reported range is likely due to the differing thermal expansion coefficients between the two phases and chemical compositions between the studies. Indeed, the Y_6Mn_{23} intermetallic (also of the G-phase structure) has been observed to exhibit an anomalous thermal expansion coefficient [37]. Therefore, the δ value is likely to vary significantly with temperature. Assuming these G-phase compositions exhibit the same thermal expansion behaviour as the previously studied G-phase structure, an estimation of the lattice parameters with temperature (using the thermal expansion coefficient for the G-phase [37] and BCC Fe [38]) can be made to estimate the temperatures at which the lattice mismatch will be zero ($T_{\delta=0\%}$) i.e. the intersect of BCC Fe and G-phase curves in Fig. A1 (appendix).

Here it is predicted that for all $X_6Ni_{16}Si_7$ compositions studied, except where X=Zr and Hf, there will be a $T_{\delta=0\%}$ value between 581 – 843 K. In theory, one could tailor the composition of the G-phase or choose a suitable ageing temperature, insofar as they both coincide, to promote nucleation. It could also be postulated that the greater the misfit, at operational temperature, the greater hardening will be present at that temperature. However, composition specific thermal expansion studies will need to be conducted for better accuracy in this prediction.

In past literature, there are fewer reports of G-phase precipitates that contain Fe instead of Ni; where this has been reported, the Fe containing G-phase was considered to be metastable. Table 3 reports the outputs obtained from G-phase structures identical to Table 2 but with Fe replacing Ni. To the authors' knowledge, no prior *ab initio* calculated data on these systems exist and, as expected, they all exhibit less favourable formation enthalpies compared to Ni-based G-phases. $T_{\delta=0\%}$ values were not calculated for these compositions due to their predicted metastability.

Most chemical composition analyses on G-phase precipitates in steels include a significant Fe content (10 – 40 at.%) [3,39,40]. Therefore, it is likely that there is a solubility limit of Fe into the $X_6Ni_{16}Si_7$ G-phase. In the $Fe_x(Mn_6Ni_{16}Si_7)_{100-x}$ system it is predicted that this limit is x = ~18 at.% [23,40].

Comparing values in table 2 and table 3 it is predicted that, in the majority of cases (with the exceptions of Ti, V and Zr), when Fe replaces Ni in the G-phase, there is an increase in the magnitude of δ. Therefore, it is perhaps favourable for an enrichment of Ni and depletion of Fe, in the G-phase, for greater ductility to be achieved in an Fe alloy.

Table 3. Lattice parameter and formation enthalpies of various G-phase precipitates with Fe.

Composition	Lattice parameter (Å)		δ (%)	Formation enthalpy (eV/formula unit)	
	Literature	Current study		Current study	$H_{Fe} - H_{Ni}$
$Cr_6Fe_{16}Si_7$	-	11.05	-2.43	-2.72	6.54
$Hf_6Fe_{16}Si_7$	-	11.38	0.49	-16.37	6.26
$Mn_6Fe_{16}P_7$	-	10.86	-4.14	-6.84	6.51
$Mn_6Fe_{16}Si_7$	-	**11.09**	**-2.05**	**-2.30**	**7.24**
$Mo_6Fe_{16}Si_7$	-	11.22	-2.05	-7.13	5.13
$Nb_6Fe_{16}Si_7$	11.33[a]	11.19	-0.85	-12.98	4.25
$Ta_6Fe_{16}Si_7$	11.29[a]	11.09	-1.16	-13.79	3.73
$Ti_6Fe_{16}Si_7$	-	11.17	-1.32	-14.36	6.04
$V_6Fe_{16}Si_7$	-	11.07	-2.27	-9.00	4.59
$W_6Fe_{16}Si_7$	-	11.05	-2.41	-6.71	4.16
$Zr_6Fe_{16}Si_7$	11.68[b]	11.44	1.06	-16.28	6.20

Experimental: [a]Rixecker *et al.* [41] [b]Wang *et al.* [42]

To identify the cause of difference in stabilities between Ni vs Fe containing G-phase compositions, the electronic structures are examined by plotting the *l*-decomposed projected density of states (PDOS) of four compositions $W_6(Ni/Fe)_{16}Si_7$ and $Zr_6(Ni/Fe)_{16}Si_7$, which represent the least and most stable non-magnetic structures, respectively, see Fig 1. The total density of states (TDOS) of all compositions are plotted in Fig. A2 and complete datasets pertaining to all *l*-decomposed $X_6(Ni/Fe)_{16}Si_7$ structures can be found in ref [43]. In all cases, there is strong hybridisation in the Si-p, Fe/Ni-d and X-s, -p and -d orbitals. The difference in stability between Ni and Fe containing compositions can be attributed to their d bands, where the former is narrower and has a higher density of states below the Fermi level (E_F). The relative stabilities between the structures containing differing X components, are also reflected by the occupancy of the d orbitals. Fig. 2 shows the relationship between the occupancy fraction of the X-d orbitals, in the upper and lower spin channels below E_F vs the formation enthalpy. The more stable G-phase compositions have lower occupancies of their d orbitals. This relationship arises due to the occupancy of the higher energy states, available in these species, leading to anti-bonding behaviour, therefore, reduced occupancy of these orbitals is energetically preferred. This is analogous to observations in previous works on crystal stability of intermetallics [44,45]. In light of these results, the trend in formation enthalpies can be loosely correlated to the number of electrons that occupy the outermost d orbital of the pure X element i.e. Hf(2)<Zr(2)<Ti(2)<Ta(3)<Nb(4)<V(3)<Mo(5)<W(4)<Mn(5)<Cr(5).

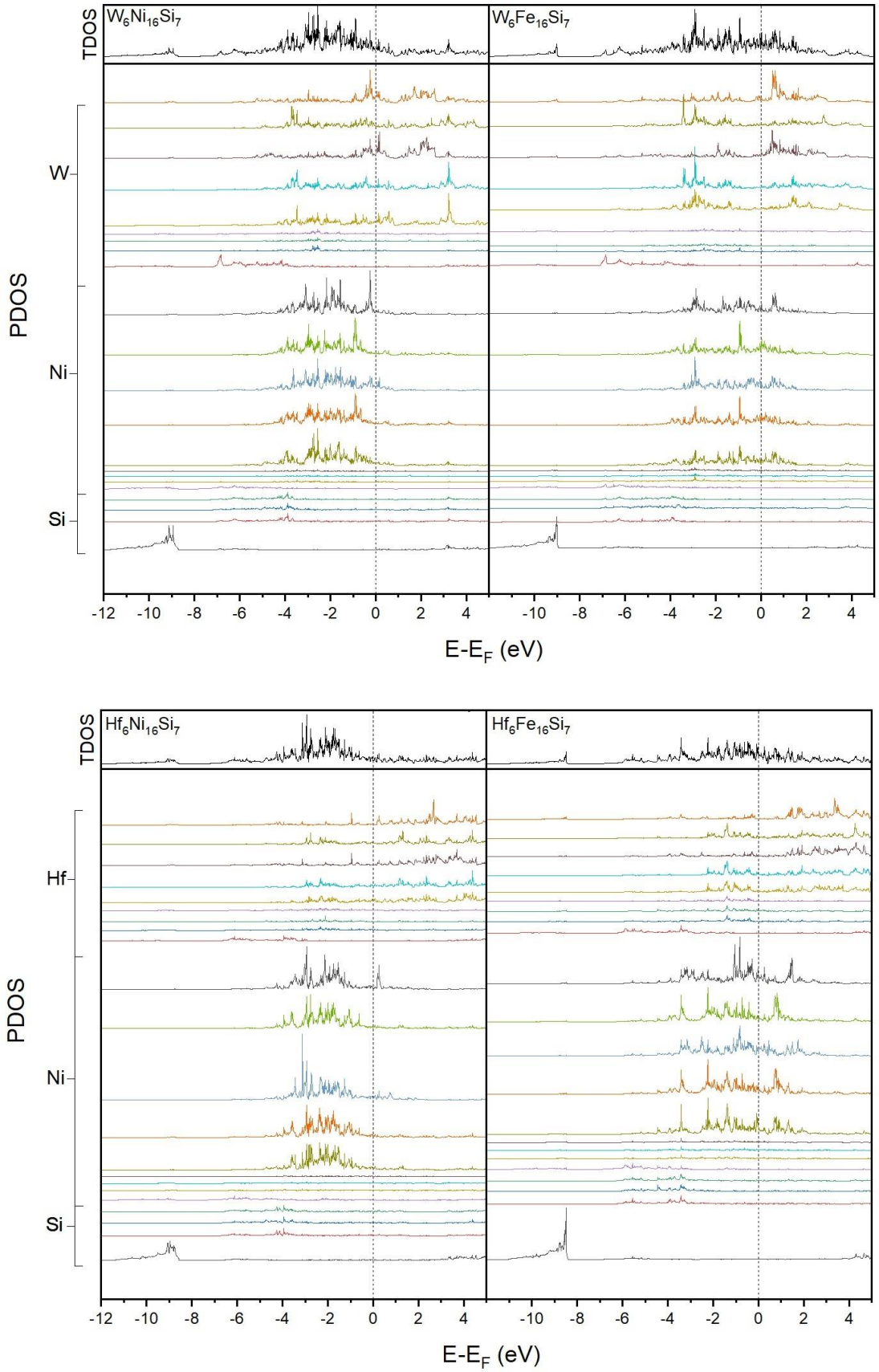


Fig 1. TDOS in the upper spin channel of four labelled G-phase compositions with their corresponding *l*-decomposed partial density of states (PDOS) below. The PDOS pertaining to each species is denoted by the section labels on the y-axis. In each section, the PDOS contribution from the s, p_y, p_z, p_x, d_{xy}, d_{yz}, d_{z2-r2}, d_{xz}, d_{x2-y2} orbital geometries are ordered from bottom to top where the d orbital is omitted for Si due to lack of available states.

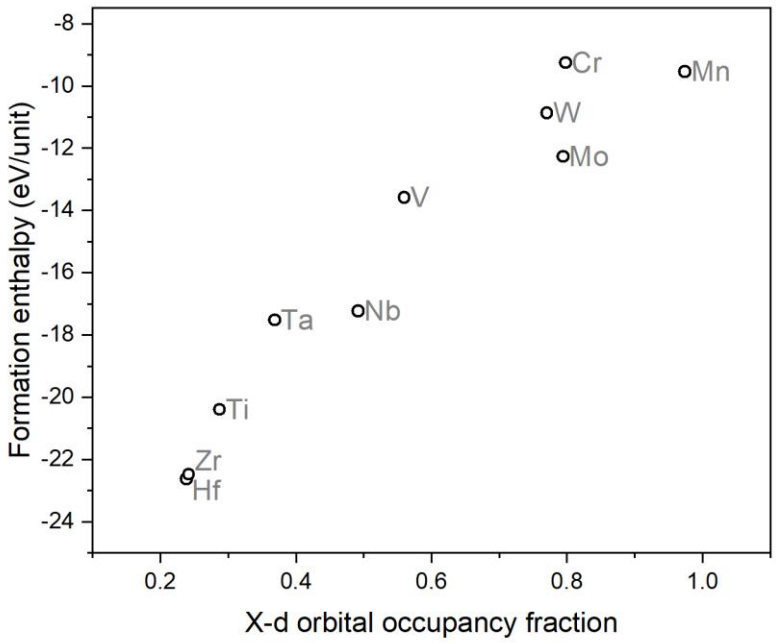


Fig 2. Relationship between the stability of each $X_6Ni_{16}Si_7$ G-phase and X-d orbital occupancy where X is labels each datapoint.

For the first time, a prediction of the elastic properties of the Ni containing G-phase structures is made from DFT, see Table 4. Pure BCC Fe is included for comparison. It is difficult to generalise the elastic properties of the G-phase structure as the results show that the bulk (*B*), shear (*E*), and Young's (G) moduli vary by a magnitude of 140.1, 37.0 and 80.3 GPa, respectively, between the different compositions (see Fig. 3). Interestingly, the $Mn_6Ni_{16}Si_7$ composition's three elastic moduli deviate the least from that of BCC Fe. It is inferred that the similarity in elastic moduli of $Mn_6Ni_{16}Si_7$ and BCC Fe may lead to reduced modulus hardening, load partitioning, debonding, and increased dislocation mobility in a ferritic steel. This could also shed some light onto the disagreement between studies in the literature that conclude that the hardening of duplex stainless steels during low-temperature annealing (~623 - 823 K) is due to either spinodal decomposition in the ferrite plus G-phase precipitation [46,47] or to spinodal decomposition alone [48]. In the former two studies, two-step hardening was observed by nanohardness measurements with age time. The first step was attributed to spinodal decomposition of α and α' phases and the second step to G-phase precipitation (identified using TEM). However, in the latter study, hardness was not measured as a function of ageing time but instead measured in three stages: (1) the wrought condition (no spinodal decomposition or G-phase in ferrite), (2) aged >10,000 h (spinodal decomposition and G-phase in ferrite), and (3) post ageing, 1 h anneal at 823 K (no spinodal decomposition but G-phase in ferrite); the hardness in the 3rd step was measured to be equal to that of the first and it was therefore concluded that it was not the G-phase that contributes to hardening. However, the former two studies measured hardness with spinodal decomposition and G-phase precipitation *combined*, whereas the latter study removed the spinodal decomposition and only observed G-phase precipitates in the matrix. Therefore, it is possible that the G-phase precipitates located at the α and α' phase boundaries increase the hardening caused by the spinodal decomposition but do not significantly contribute to hardening when precipitating in the ferrite matrix; a hypothesis that the DFT results within the current study supports. The caveat to this is that the composition and/or precipitate sizes differ significantly between both studies, which is possible due to the lack of data pertaining to these quantities.

Table 4. Calculated elastic constants of Ni containing G-phase precipitates examined within this study.

Composition	**C_{11} (GPa)**	**C_{12} (GPa)**	**C_{44} (GPa)**	***B* (GPa)**	***G* (GPa)**	***E* (GPa)**	***v***	***B/G***
BCC Fe	270.2	136.6	89.8	181.0	79.5	208.1	0.31	2.30
$Cr_6Ni_{16}Si_7$	246.1	76.0	90.6	132.7	88.3	216.8	0.23	1.50
$Hf_6Ni_{16}Si_7$	316.6	90.0	102.8	165.5	106.9	263.9	0.23	1.55
$Mn_6Ni_{16}P_7$	232.8	44.9	89.0	107.5	91.0	212.8	0.17	1.18
$Mn_6Ni_{16}Si_7$*	288.4	122.3	96.7	177.8	91.0	233.2	0.28	1.95
$Mo_6Ni_{16}Si_7$*	354.8	172.9	103.6	233.6	98.3	258.8	0.32	2.38
$Nb_6Ni_{16}Si_7$*	358.6	134.8	113.6	209.4	112.9	287.1	0.27	1.85
$Ta_6Ni_{16}Si_7$	388.4	151.6	120.0	203.8	116.3	293.1	0.26	1.75
$Ti_6Ni_{16}Si_7$*	345.5	127.4	104.9	200.0	106.5	271.4	0.27	1.88
$W_6Ni_{16}Si_7$	377.5	182.7	109.4	247.6	104.4	274.6	0.32	2.37
$Zr_6Ni_{16}Si_7$	301.4	87.3	93.6	158.7	98.8	245.4	0.24	1.61

*Slightly overestimated (~10%) due to exclusion of ionic contributions.

In five of the structures (denoted by * in Table 4), the energy landscape surrounding the atomic positions of the X component were too shallow to calculate the displacement response internal strain tensor. Therefore, the ionic contributions to the elastic constants were not included. These are estimated to be one order of magnitude smaller than the frozen-ion elastic tensor and negative. For a full breakdown of the contributions refer to ref. [43].

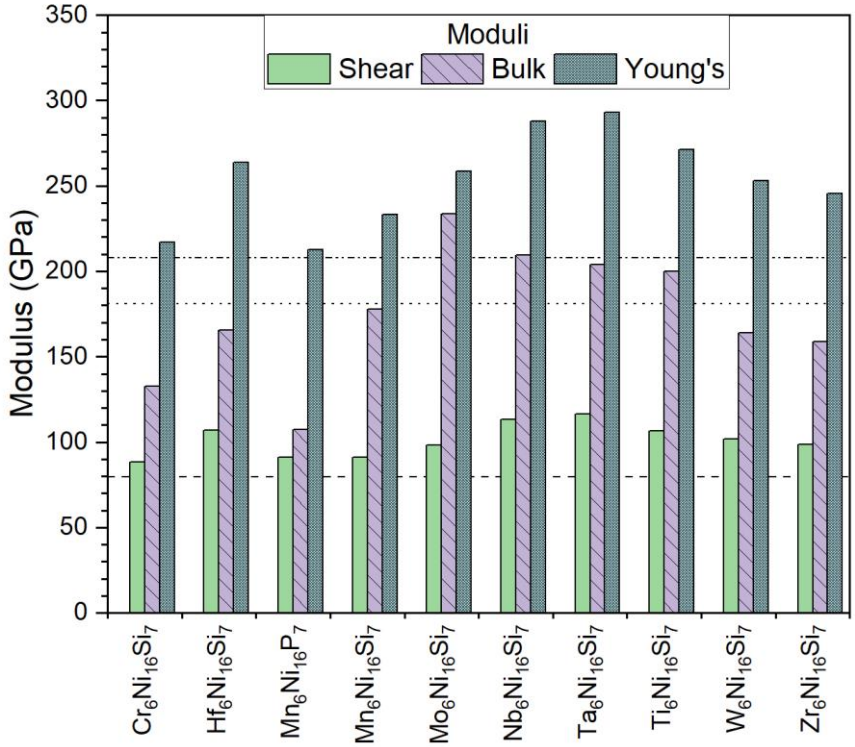


Fig 3. Shear (open green bars), bulk (striped purple bars) and Young's (blue thatched bars) moduli for all Ni containing G-phase compositions examined in this study. Comparison to the shear (dashed line), bulk (dotted line) and Young's (dot dashed line) moduli for pure BCC Fe included.

3.2 Substitution from BCC Fe into the $Mn_6Ni_{16}Si_7$ G-phase

The G-phase has five unique lattice sites: 1 Mn, 2 Ni and 2 Si, here labelled Mn, Ni1, Ni2, Si1 and Si2, see Fig. 4. In this section, the substitution energies of 14 elements and a vacancy, when substituted onto these sites in the 116 atom cubic G-phase unit cell (corresponding to concentrations of 0.86 at.%), are presented.

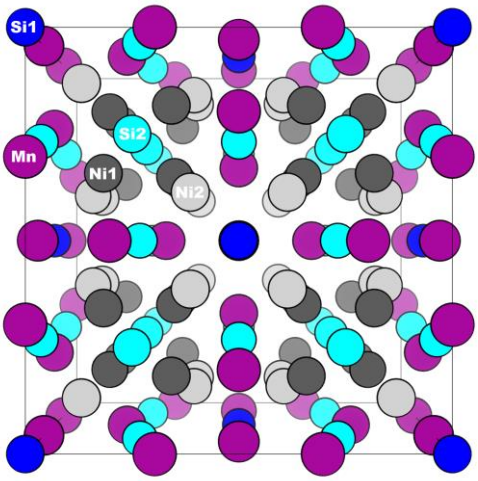


Fig. 4. The 116 atom cubic G-phase unit cell showing the equivalent Mn (purple), Ni1 (dark grey), Ni2 (light grey), Si1 (dark blue) and Si2 (light blue) lattice sites.

Instead of the typical calculation of substitution energy, where the reference structure of the species substituting is taken as their ground state pure form, here the reference structure is taken as their solution in BCC Fe and a negative substitution energy indicates an exothermic reaction. A comparison between the results using the conventional method and current method is shown in Fig. A3.

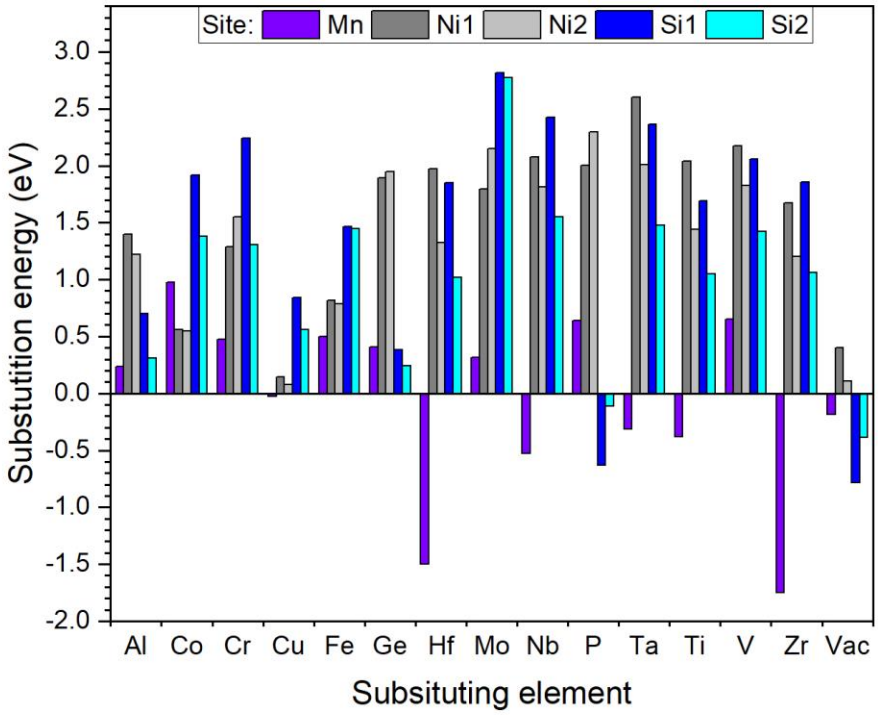


Fig 5. Substitution energy of each element from BCC Fe to the Mn (1st column), Ni1 (2nd column), Ni2 (3rd column), Si1 (4th column) and Si2 (5th column) in the $Mn_6Ni_{16}Si_7$ G-phase structure.

Fig. 5 shows the results for 14 different species, and a vacancy onto the five unique lattice sites of the G-phase. Some of the X metals e.g. Hf, Zr and Ti, which were predicted to form low energy (more stable) G-phases, have a large energetic preference for the Mn site (Zr>Hf>Nb>Ti>Ta) and it is expected that the inclusion of these species in the melt will significantly promote G-phase formation. Interestingly, of the X metals that form low energy G-phases, Mo and V do not display this behaviour in substitution; in the case of the latter element, this is due to the stability of V in the BCC Fe lattice evidenced by the large solubility in their binary phase diagram [49]. The behaviour of Mo is less clear and its influence

on G-phase precipitation has been a topic of experimental investigation in stainless steels, in the past. The state-of-the-art theory suggests that Mo promotes G-phase formation through expediting the kinetic process of spinodal decomposition between α and α' phases, leading to larger cross-flow of Mn, Ni and Si [50]. However, a systematic study on the effect of Mo in low alloy ferritic steels has not been conducted to-date. The results presented here suggest that, at low concentrations (<1 at.%), Mo will not show a preference for substitution onto the Mn-Ni-Si G-phase over a pure BCC Fe matrix, therefore, will not promote G-phase formation. Observations of Mo concentrations between 0.14 – 3.6 at.% in the Mn-Ni-Si G-phase have been made in low Mo stainless steels. We attribute this discrepancy between the results within the current study and past experiment to be due to the difference in chemical composition of the α/α'-Fe phases, in stainless steel, to the pure BCC Fe phase modelled here, and/or diffusion kinetics and entropic contributions not considered by DFT.

Cu is predicted to have a slight preference for substitution onto the Mn site, and the substitution energy onto both the Ni sites is also very small. The clustering of Cu, Mn, Ni, and Si is a well-known degradation phenomenon in RPV steels [51–53]. Therefore, it is no surprise that there is favourable Cu accommodation in the G-phase. However, Cu precipitation (in the absence of Mn, Ni and Si) is also a well-known phenomenon in thermally aged steels [54–56] and is expected to take preference over the substitution into the G-phase.

Another interesting finding is the preference for P to substitute onto the Si lattice sites. Again, another species known to cluster with Mn, Ni and Si in RPV steels, and segregate to grain boundaries [57]. It is possible that the affinity of P for the G-phase contributes to the preferential precipitation of the G-phase at grain boundaries in steel.

Vacancies show a unique behaviour in substitution preference. In the G-phase structure they are much more stable than in BCC Fe when situated on the Si1>Si2>Mn lattice sites. These results suggest that the G-phase could act as a sink for vacancies, and offers an explanation for the observed reduction in Si content from its stoichiometric composition in chemical analyses from past experimental studies [9,40,58].

Fe and Cr are two species that feature heavily in G-phase chemical analyses, yet both are predicted to be unfavourable when substituted into the G-phase from a BCC Fe matrix. This result supports the observation of a decrease in Fe and Cr content in G-phase precipitates with ageing time in past studies [50,59]. However, as previously stated, the differing chemical environments due to the alloy composition in stainless steels i.e. high availability of Fe and Cr and deficiency of Mn, Ni and Si, it is likely that an equilibrium concentration of Fe and Cr could exist in the G-phase structure.

Unexpectedly, the most favourable site for Fe to occupy is the Mn site. It has long been assumed that Fe will occupy the Ni site, and most recently theorised that it will occupy the Si lattice site [40]. The results shown here suggest the former assumption incorrect and the latter theory has been recently contested by our group [60].

3.2 $Fe_{x+y+z}Mn_{6-x}Ni_{16-y}Si_{7-z}$ formation energies

To determine the effect of large concentrations (~12 at.%) of Fe on the stability of Mn-Ni-Si G-phase and BCC structure, 14 Fe atoms were substituted for each species and their site occupations were randomised ten times to obtain a sample of the effect of disorder on a G-phase lattice and BCC packed arrangement, respectively. The concentration of Fe was chosen as it has previously been predicted, to be at the threshold at which point the G-phase structure and BCC packing are equal in formation enthalpy [23,40].

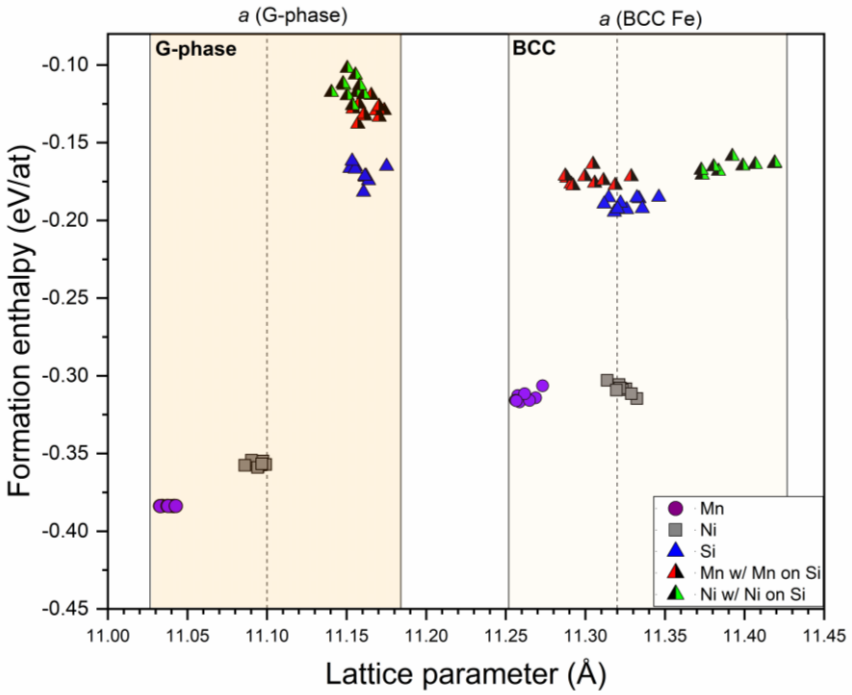


Fig 6. Formation enthalpies and lattice parameters of Fe-Mn-Ni-Si containing compositions of G-phase (left shaded area) and BCC (right shaded area). 14 Fe replace Mn (circles), Ni (squares), Si (open triangles) lattice sites in the 116 and 128 atom unit cell of G-phase and BCC structure, respectively, and ten randomisations of occupancies were performed for each. Additional simulations were performed for fixed composition $Fe_{3.5}Mn_6Ni_{16}Si_{3.5}$ where Fe displaces Mn and Mn occupies Si sites (left open triangles) and Fe displaces Ni and Ni occupies Si sites (right open triangles).

Fig. 6 shows the formation energy and lattice parameter of each G-phase and BCC packed structures simulated with an Fe concentration of ~12 at.%. In the G-phase, a trend in site preference, similar to the single Fe atom substitutions, is found i.e. Mn>Ni>Si in favourability. In the BCC packed system there is no clear favourability for Fe to occupy Ni or Mn sites, however, replacement of the Si site remains relatively unfavourable. Interestingly, when Fe replaces Ni or Si in the BCC packed structures, the lattice parameters deviate the least from a pure BCC matrix (dashed vertical line). From this result we may deduce that the maintenance of stoichiometric Mn will minimise the misfit between a BCC packed cluster and the surrounding Fe matrix. Conversely, the replacement of Mn with Fe will lead to a significantly smaller volume, which may also be associated with an energy penalty for small clusters in an Fe matrix. This may explain recent observations by Almirall *et al.* of the proportionality between number density of "Mn-Ni-Si precipitates" and Mn contents of the base steel [61]. Moreover, when Fe replaces Si, the G-phase is no longer predicted to be more favourable than the BCC packing. This is a logical outcome as G-phase is a silicide.

Additional simulations were carried out on compositions more similar to cluster/G-phase compositions experimentally observed in low alloy and stainless steels, i.e. reduced Si content [9,40,58]. Two situations were considered: 14 Fe occupying the (1) Mn site and the displaced Mn atoms occupying the Si sites (left open triangles), and (2) Ni site with the displaced Ni atoms again occupying the Si sites (right open triangles). The results from these additional simulations show that, when the compositions are kept consistent, the trend of site preference of Fe is changed. Indeed, it is possible that Fe will preferentially occupy the Si lattice site due to the chemical availability of species offering an additional explanation to the findings of Matsukawa *et al.* [40,60]. Therefore, it is predicted that the initial steel composition and ratio of solute species will affect the site preference of Fe and overall composition of the G-phase and solute clusters in steels. The latter of which has also recently been concluded experimentally [62].

3.2 Promotion of the G-phase

The promotion of G-phase precipitation is not historically designed for in a steel. Due to the context of past investigations, long ageing times are typically performed (2,500 – 200,000 h [59]), to simulate components in long service operation. As far as we are aware it is only in two recent publications [12,28] where investigations into the promotion of G-phase, for strengthening of an Fe alloy, is documented. In this context, reducing the required ageing time is of great interest. Another desirable property for a precipitate hardened alloy is maintenance in ductility. To optimise an Fe alloy composition to for these two traits we employed the following design principles:

1. Addition of Mn to promote $Mn_6Ni_{16}Si_7$ formation, predicted to be similar in elastic properties to an α-Fe matrix, to try to preserve ductility.
2. Addition of Zr to promote $(Mn,Zr)_6Ni_{16}Si_7$ to expedite G-phase nucleation by decreasing enthalpy of formation, increasing precipitation temperature, and offsetting negative δ value between G-phase and α-Fe matrix at room temperature.

Other design principles include: addition of Cr for oxide scale, omission of other embrittling intermetallic phases other than G-phase, limitation of Si to 6.7 at.% to avoid potential loss of workability, and annealing temperature ≥700 K to expedite kinetics.

In this study, CALPHAD was used to explore the phase space of an Fe alloy containing Cr, Ni, Si, Mn and Zr, by varying contents in step sizes of 1.0 at.% for the first three elements, and 0.1 at% for MnZr, in the $Fe_{bal}Cr_8Ni_3Si_3(Mn_{0.5}Zr_{0.5})_{1.2}$ system. This was done to predict a suitable composition and aging temperature, to achieve the largest phase fraction of G-phase and avoid other intermetallic phases, for the proceeding experimental section of this study. The property diagram of the optimised alloy is presented in Fig. 7. At equilibrium, it is predicted that a dual phase BCC Fe and G-phase could exist between 700 and 800 K. This is labelled as the "region of interest". Below 700 K, additional phases: σ-FeCr, a second BCC Fe phase, and Cr_3Si are also predicted to form. Above 800 K, γ-Fe FCC phase, and Fe_2Zr Laves phase are predicted to form.

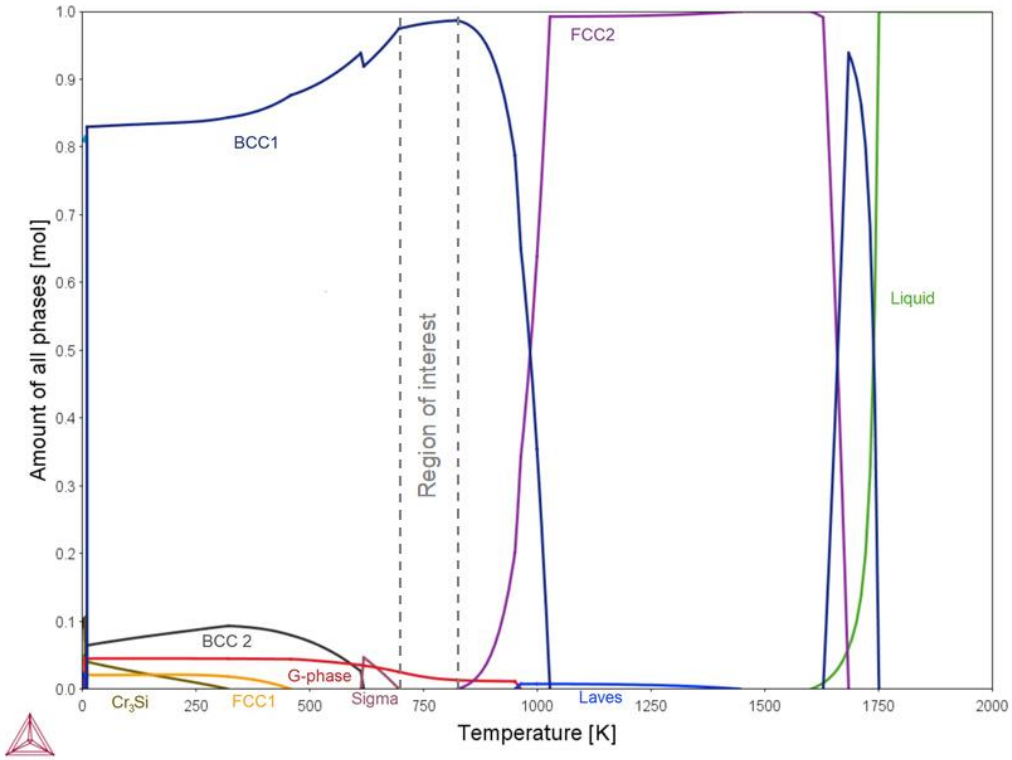


Fig. 7. Property diagram of $Fe_{bal}Cr_9Ni_4Si_2(Mn_{0.6}Zr_{0.4})_{1.1}$ wt.% ($Fe_{bal}Cr_9Ni_4Si_4[Mn_{0.6}Zr_{0.4}]_{1.2}$ at.%) using TCFE7 database in Thermocalc. Region of interest enclosed by dashed lines at 700 and 800 K.

The effect of varying each elemental species in the mixture on the size of this region of interest is graphically represented in Fig. 8. As Cr is added to the mixture, it is predicted that there will be a significant phase fraction of σ-FeCr that forms at ~500 K, which shifts to higher temperatures until 13 at.% at which point it completely overlaps with the dual phase forming region. The addition of Si past 6.7 at.% (3.5 wt.%) has been shown to greatly reduce workability of a steel [63] and therefore results for Si > 6 at.% were not included. However, Si addition is predicted to have a large influence on the increase in upper bounds of the BCC Fe and G-phase dual phase forming region. The influence of Ni is pronounced, when < 2 at.% there is no dual phase forming region due to Laves phase precipitation, which is suppressed to higher temperatures with the addition of Ni to contents between 2-4 at.%. When > 4 at.%, the lower bounds of the γ-Fe phase extends to 600 K. It is recognised that a duplex BCC+FCC microstructure may be desirable for some applications, in which case an increase in Ni is predicted to promote this. Finally, the addition of MnZr in equal portions is possible between 0.1 – 1.0 at.% at which point σ-(Fe,Mn)Cr phase and the Fe_2Zr Laves phase will prevent the formation of a dual phase BCC Fe and G-phase region. It was determined that when Mn and Zr were each included above 0.6 at.% (1.2 at.% total) the phase fraction was at its maximum.

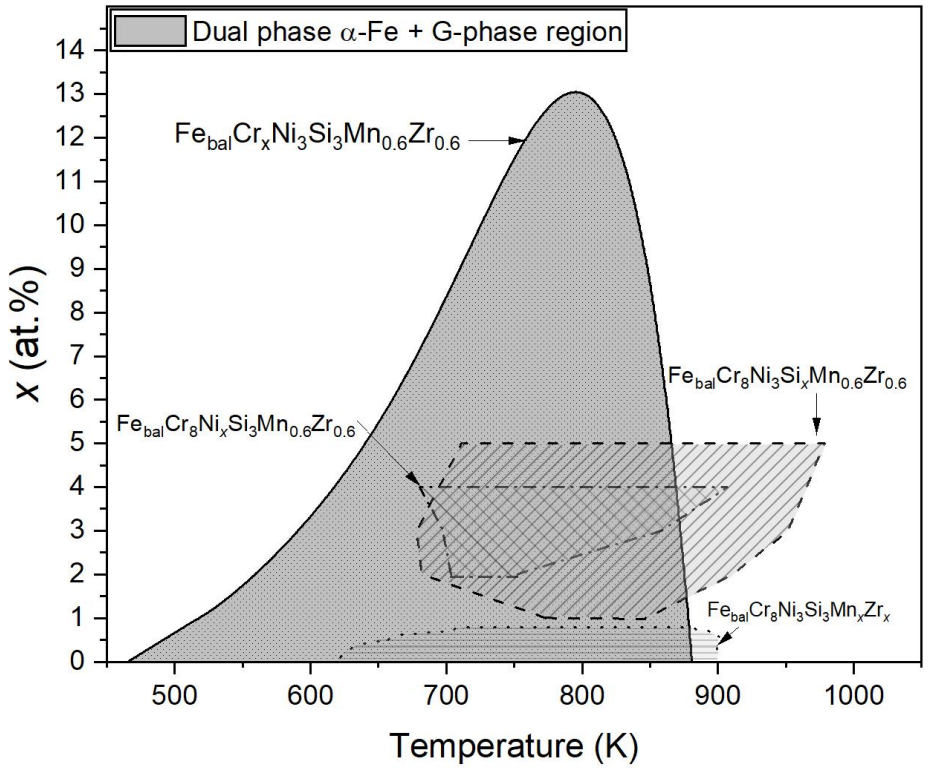


Fig 8. Dual G-phase + BCC Fe phase forming regions when Cr (solid line), Ni (dot dashed line), Si (dashed line) and MnZr (dotted line) are varied in the $Fe_{bal}Cr_9Ni_3Si_3(Mn_{0.5}Zr_{0.5})_{1.2}$ at.% system.

From the previous analysis of lattice misfit (δ) in the current study, it can be postulated that an equal ratio of Mn and Zr in the G-phase will lead to a minimisation of δ. The fraction of Mn in a hypothetical $[Mn_{x'}Zr_{(1-x')}]_6Ni_{16}Si_7$ precipitate, in the optimised alloy $Fe_{bal}Cr_9Ni_4Si_4[Mn_xZr_{(1-x)}]_{1.2}$ at.%, where x is the fraction Mn contributing to the 1.2 at.% total of Mn+Zr included in the initial mixture and x' is the ratio of Mn:Zr predicted in the G-phase precipitate by Thermocalc, see Fig 9. It is predicted that there will be a depletion of Mn and enrichment of Zr in the G-phase for higher temperatures. When included in a 1:1 ratio (0.6:0.6), there is no temperature at which it is predicted that an equal ratio will be achieved in the G-phase. However, when increasing the Mn:Zr ratio to 3:2 (0.72:0.48) an equal concentration of both species is predicted to occur at 645 K. A higher portion of Mn is also retained at higher temperatures compared to the other tested ratios. When the Mn:Zr ratio is increased further to 4:1 (0.96:0.24) the dual phase region is greatly reduced to 636 K due to FCC phase formation.

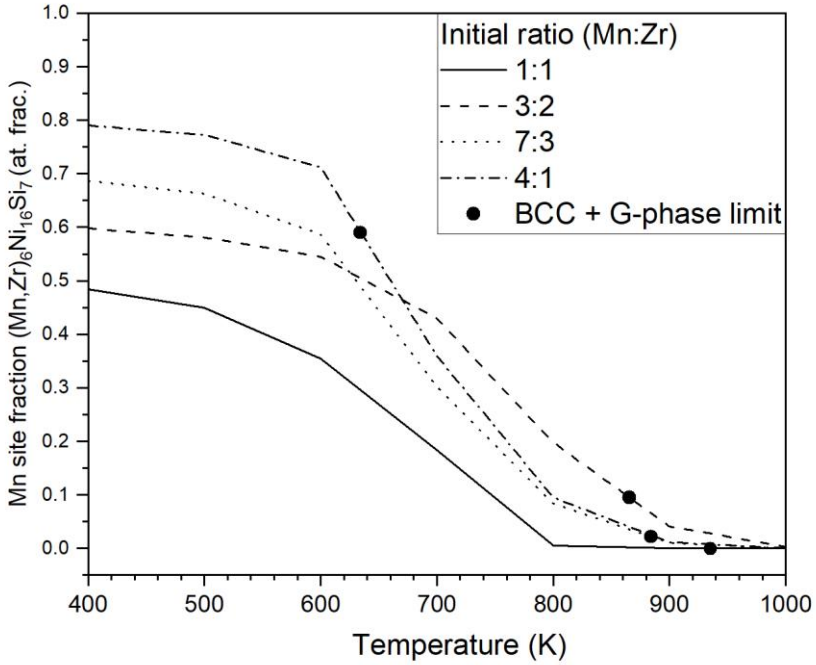


Fig. 9. Thermocalc predictions of the site fraction of Mn in the $(Mn,Zr)_6Ni_{16}Si_7$ G-phase formed from the $Fe_{bal}Cr_9Ni_3Si_3(MnZr)_{1.2}$ mixture with initial atomic ratios of Mn:Zr as 1:1 (solid line), 3:2 (dashed line), 7:3 (dotted line) and 4:1 (dot dashed line) with the BCC + G-phase forming limit denoted on each line by a solid circle.

From the results within this study, it is possible to conclude that concentrations of 4 at.% Ni, 5 at.% Si, 0 at.% Cr and 1.2 at.% (Mn, Zr) yield the highest upper bounds of the dual phase forming regions. However, in the interest of including a Cr content high enough for reasonable oxidation/corrosion resistance behaviour (~9 at.% minimum [64]), and maintaining a high portion of Mn in the G-phase with lowest δ value at room temperature, we arrive at the composition ($Fe_{81.4}Cr_9Ni_4Si_2[Mn_{0.6}Zr_{0.4}]_{1.2}$) at.%.

3.2 Experimental analysis of predicted alloy

The casting and heat treatments of the predicted composition, $Fe_{81.4}Cr_9Ni_4Si_2[Mn_{0.6}Zr_{0.4}]_{1.1}$ (wt.%), revealed remarkable promise. Fig. 10 displays the micro-hardness with ageing time (at 773 K) of the predicted composition and compares to two other compositions: $Fe_{bal}Ni_7Si_2Mn_1$ and $Fe_{Bal}Cr_{20}Ni_3Si_3Mn_1$ (wt.%).

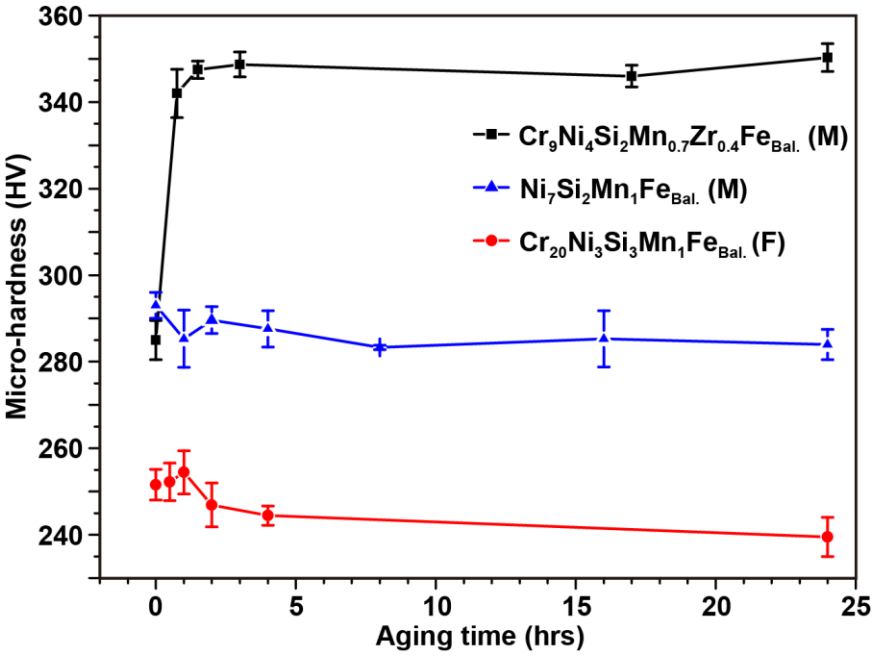


Fig. 10. The micro-hardness with ageing time of $Fe_{bal}Cr_9Ni_4Si_2Mn_{0.7}Zr_{0.4}$ (squares), $Fe_{bal}Ni_7Si_2Mn_1$ (triangles), and $Cr_{20}Ni_3Si_3Mn_1Fe_{bal}$ (circles) alloys (wt%). With lines to guide the eye and labels M and F, which represent observed martensitic and ferritic microstructures, respectively. Error bars show standard deviation.

Hardening of ~60 HV occurs extremely quickly (~1 h) for the predicted composition, whereas hardening does not occur for the other alloys within the 24 h tested. Fig. 11 presents the TEM analysis of the predicted composition after 24 h of ageing. Lath martensite with a high dislocation density is observed, which is due to the initial quenching of the alloy from high temperature (1475 K) austenite. Fine precipitates, ~1 nm in diameter, were observed dispersed within the martensitic phase. The selected area electron diffraction pattern of this region revealed a double diffraction pattern of a G-phase structure with a cube-on-cube orientation with a BCC phase. No such precipitation was observed in the other two compositions, see Fig. A4.

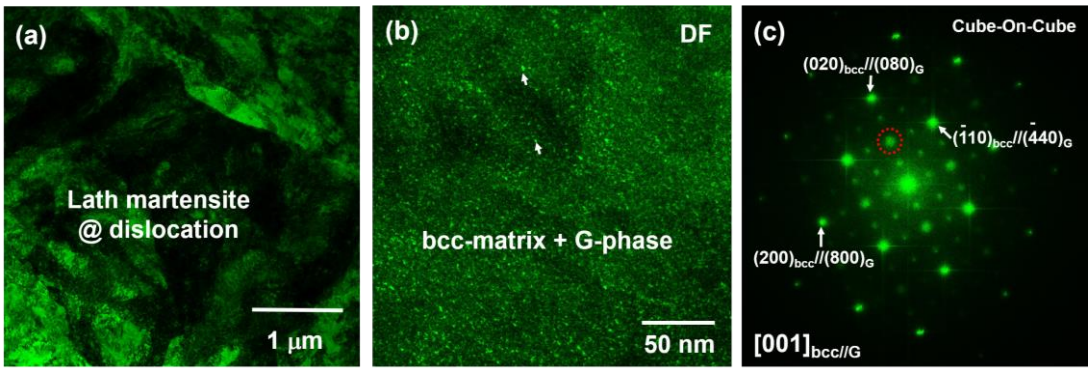


Fig. 11. TEM dark field images of the microstructure showing nanoscale G-phase precipitates in the predicted $Fe_{bal}Cr_9Ni_4Si_2Mn_{0.7}Zr_{0.4}$ alloy after ageing at 773 K for 24 h at (a) low magnification, (b) higher magnification, and (c) selected area electron diffraction pattern. Where (b) is taken from the 040G spot in (c) (dotted circle).

From these results it is reasonable to deduce that the addition of Zr to the composition expedited G-phase precipitation. As far as the authors are aware, the shortest ageing time before that showed a $Mn_6Ni_{16}Si_7$ G-phase precipitate is 500 h at 750 K [46], therefore a result of $\leq$ 24 h is significant. However, it is noted that chemical analysis is still required to confirm the chemistry of the precipitates. A technique such as atom probe tomography (APT) that has higher resolution is required, however that was not within the scope of this study.

The lattice parameter of the BCC phase formed in the predicted composition was measured to be 0.286 nm. Due to the small scale of the precipitates an accurate lattice parameter could not be obtained, however, from the observed cube-on-cube orientation we can assume it to be close to that of the matrix ,

which would equate to a G-phase lattice parameter of ~1.144 nm. Coherency and low interfacial energy between the two phases could explain the lack of merging/coarsening of precipitates but it is also possible that there exists a strain energy suggested by the streaking of the diffraction spots in Fig. 11(c), which would also supress coarsening.

4. Conclusions

A combination of theory and experiment were used to design and test a new Fe alloy composition [$Fe_{bal}Cr_9Ni_4Si_2(Mn_{0.6}Zr_{0.4})_{1.2}$ at.%] that expedites the formation of the G-phase, as a strengthening phase, with coherency with to the BCC Fe matrix, and avoid Laves phase precipitation. The following conclusions can be drawn from this work:

- The combination of Mn and Zr as a shared X component in the $X_6Ni_{16}Si_7$ G-phase precipitate leads to large reduction in precipitation time ($\leq$ 24 h) and coherency within a BCC Fe matrix, with an associated hardening of ~60 HV that occurs after ~1 h at 773 K.
- In general, G-phase formation in steel is best promoted by including Ni, Si, and at least one other element of species Hf, Zr, Ti, Ta, Nb, V, Mo, W, Mn, Cr (in order of decreasing energetic favourability). The differing magnitudes of energies of formation of these species is proportional to the occupancy of the d-band when in the G-phase structure.
- The $Mn_6Ni_{16}Si_7$ G-phase is predicted to have the most similar elastic properties to BCC Fe and therefore minimise the G-phase nucleation barrier, modulus hardening, load partitioning, debonding, and increase dislocation mobility in a BCC Fe matrix. A mixture of Mn:Zr in 3:2 ratio should be included to allow for an increased ageing temperature to expediate precipitation.
- There is a high energetic preference for vacancies to occupy the G-phase Si lattice sites displacing Si to the BCC Fe phase. Therefore, the G-phase will act as a vacancy sink and reduction of Si content from stoichiometric composition will be observed.
- The concentration of species available in the alloy mixture is predicted to affect the solubility of Fe into the G-phase and stability of the G-phase relative to a concentrated BCC packed structure. When there is excess Si available, Fe will preferentially substitute onto the Mn or Ni sites. However, when deficient in Si (half stoichiometric G-phase), the preference for Fe substitution changes to the Si sites, which decreases the favourability of a G-phase over a BCC structure. If the suppression of the G-phase is desired, it is recommended that Si is kept as low as possible in the alloy mixture.

Acknowledgements

Mark Wenman and Daniel King were funded by EPSRC grant no. EP/P005101/1. Thomas Whiting acknowledges support through the CDT in nuclear energy grant no. EP/L015900/1 and funding from Rolls-Royce Plc. Mujin Yang and Xingjun Liu were funded by the National Natural Science Foundation of China (Grant No. 51971082). This research was undertaken with the assistance of resources provided by the Australian National Computational Infrastructure (Raijin) supported by UNSW, Tier 2 EPSRC resource allocation on Cambridge computing facilities (CSD3), and Imperial College Tier 2 computing (Cx1 and Cx2).

References

[1] H.D. Solomon, L.M. Levinson, Mössbauer effect study of '475 C embrittlement'of duplex and ferritic stainless steels, Acta Metall. 26 (1978) 429–442.

[2] P. Auger, F. Danoix, A. Menand, S. Bonnet, J. Bourgoin, M. Guttmann, Atom probe and transmission electron microscopy study of aging of cast duplex stainless steels, Mater. Sci. Technol. 6 (1990) 301–313.

[3] A. Mateo, L. Llanes, M. Anglada, A. Redjaimia, G. Metauer, Characterization of the intermetallic G-phase in an AISI 329 duplex stainless steel, J. Mater. Sci. 32 (1997) 4533–4540.

[4] X. Yan, A. Grytsiv, P. Rogl, V. Pomjakushin, X. Xue, On the crystal structure of the Mn–Ni–Si G-phase, J. Alloys Compd. 469 (2009) 152–155.

[5] H.J. Beattie, F.L. VerSnyder, A new complex phase in a high-temperature alloy, Nature. 178 (1956) 208–209.

[6] E.A. Kenik, T. Inazumi, G.E.C. Bell, Radiation-induced grain boundary segregation and sensitization of a neutron-irradiated austenitic stainless steel, J. Nucl. Mater. 183 (1991) 145–153.

[7] F. Danoix, P. Auger, D. Blavette, An atom-probe investigation of some correlated phase transformations in Cr, Ni, Mo containing supersaturated ferrites, Surf. Sci. 266 (1992) 364–369.

[8] W. Xiong, H. Ke, R. Krishnamurthy, P. Wells, L. Barnard, G.R. Odette, D. Morgan, Thermodynamic models of low-temperature Mn – Ni – Si precipitation in reactor pressure vessel steels, MRS Commun. 4 (2014) 101–105.

[9] D.J. Sprouster, J. Sinsheimer, E. Dooryhee, S.K. Ghose, P. Wells, T. Stan, N. Almirall, G.R. Odette, L.E. Ecker, Structural characterization of nanoscale intermetallic precipitates in highly neutron irradiated reactor pressure vessel steels, Scr. Mater. 113 (2016) 18–22.

[10] S.J. Zinkle, G.S. Was, Materials challenges in nuclear energy, Acta Mater. 61 (2013) 735–758.

[11] M. Yang, C. Wang, S. Yang, Z. Shi, X. Liu, New insights into the precipitation strengthening of ferritic steels: Nanoscale G-phase particle, Mater. Lett. 209 (2017) 134–137.

[12] W.W. Sun, R.K.W. Marceau, M.J. Styles, D. Barbier, C.R. Hutchinson, G phase precipitation and strengthening in ultra-high strength ferritic steels: towards lean 'maraging'metallurgy, Acta Mater. 130 (2017) 28–46.

[13] M. Yang, J. Zhu, C. Wu, S. Yang, Z. Shi, C. Wang, X. Liu, Microstructural evolution and precipitation strengthening in a new 20Cr ferritic trial steel, Mater. Sci. Eng. A. 742 (2019) 734–742.

[14] S. Jiang, H. Wang, Y. Wu, X. Liu, H. Chen, M. Yao, B. Gault, D. Ponge, D. Raabe, A. Hirata, M. Chen, Y. Wang, Z. Lu, Ultrastrong steel via minimal lattice misfit and high-density nanoprecipitation, Nature. 544 (2017) 460.

[15] J.M. Vitek, G-phase formation in aged type 308 stainless steel, Metall. Trans. A. 18 (1987) 154–156.

[16] G. Kresse, J. Furthmüller, Software VASP, vienna (1999), Phys. Rev. B. 54 (1996) 169.

[17] G. Kresse, D. Joubert, From ultrasoft pseudopotentials to the projector augmented-wave method, Phys. Rev. B. 59 (1999) 1758.

[18] M. Methfessel, A.T. Paxton, High-precision sampling for Brillouin-zone integration in metals, Phys. Rev. B. 40 (1989) 3616.

[19] J.P. Perdew, K. Burke, M. Ernzerhof, Generalized gradient approximation made simple, Phys. Rev. Lett. 77 (1996) 3865.

[20] P.E. Blöchl, O. Jepsen, O.K. Andersen, Improved tetrahedron method for Brillouin-zone integrations, Phys. Rev. B. 49 (1994) 16223.

[21] Y. Le Page, P. Saxe, Symmetry-general least-squares extraction of elastic data for strained materials from ab initio calculations of stress, Phys. Rev. B. 65 (2002) 104104.

[22] G. Grimvall, Thermophysical properties of materials, Elsevier, 1999.

[23] D.J.M. King, P.A. Burr, S.C. Middleburgh, T.M. Whiting, M.G. Burke, M.R. Wenman, The formation and structure of Fe-Mn-Ni-Si solute clusters and G-phase precipitates in steels, J. Nucl. Mater. 505 (2018) 1–6.

[24] S.C. Middleburgh, D.M. King, G.R. Lumpkin, M. Cortie, L. Edwards, Segregation and migration of species in the CrCoFeNi high entropy alloy, J. Alloys Compd. 599 (2014) 179–182.

[25] D.M. King, S.C. Middleburgh, L. Edwards, G.R. Lumpkin, M. Cortie, Predicting the Crystal Structure and Phase Transitions in High-Entropy Alloys, Jom. 67 (2015) 2375–2380.

[26] D.J.M. King, S.C. Middleburgh, A.G. McGregor, M.B. Cortie, Predicting the formation and stability of single phase high-entropy alloys, Acta Mater. 104 (2016) 172–179.

[27] D.J.M. King, P.A. Burr, E.G. Obbard, S.C. Middleburgh, DFT study of the hexagonal high-entropy alloy

fission product system, J. Nucl. Mater. 488 (2017) 70–74.
[28] M. Yang, J. Zhu, T. Yang, J. Luan, Z. Jiao, X. Fan, B. Kuhn, X. Xiong, C. Wang, C.T. Liu, A novel ferritic steel family hardened by intermetallic compound G-phase, Mater. Sci. Eng. A. 745 (2019) 390–399.
[29] P.H.T. Philipsen, E.J. Baerends, Cohesive energy of 3d transition metals: density functional theory atomic and bulk calculations, Phys. Rev. B. 54 (1996) 5326.
[30] K. Lejaeghere, V. Van Speybroeck, G. Van Oost, S. Cottenier, Error estimates for solid-state density-functional theory predictions: an overview by means of the ground-state elemental crystals, Crit. Rev. Solid State Mater. Sci. 39 (2014) 1–24.
[31] E.I. Gladyshevskii, P.I. Kripyakevich, Y.B. Kuz'ma, The crystal structure of low-silicon ternary compounds in the Cr− Ni− Si and Cr− Co− Si systems, J. Struct. Chem. 3 (1962) 402–410.
[32] A. Grytsiv, X.-Q. Chen, P. Rogl, R. Podloucky, H. Schmidt, G. Giester, V. Pomjakushin, Crystal chemistry of the G-phases in the {Ti, Zr, Hf}–Ni–Si systems, J. Solid State Chem. 180 (2007) 733–741.
[33] P. Chaudouet, R. Madar, R. Fruchart, B. Lambert, Etude de nouveaux pnictures ternaires de metaux de transition isostructuraux des phases G, Ni16Mn6P7, Ni16Mn6As7, Mater. Res. Bull. 18 (1983) 713–719.
[34] Y.B. Kuzma, E.I. Gladyshevskii, E.E. Cherkashin, The Mn-Ni-Si System, Russ. J. Inorg. Chem. 9 (1964) 1028–1031.
[35] K.L. Holman, E. Morosan, P.A. Casey, L. Li, N.P. Ong, T. Klimczuk, C. Felser, R.J. Cava, Crystal structure and physical properties of Mg6Cu16Si7-type M6Ni16Si7, for M= Mg, Sc, Ti, Nb, and Ta, Mater. Res. Bull. 43 (2008) 9–15.
[36] J. Bentley, M.K. Miller, Combined atom-probe and electron microscopy characterization of fine scale structures in aged primary coolant pipe stainless steel, MRS Online Proc. Libr. Arch. 82 (1986).
[37] E. Gratz, D. Gurjazkas, H. Müller, A. Kottar, I.S. Dubenko, S.A. Granovsky, A.S. Markosyan, Anomalous thermal expansion in YMn2, Y6Mn23 and YMn12, Phys. B Condens. Matter. 237 (1997) 474–475.
[38] Z.S. Basinski, W. Hume-Rothery, A.L. Sutton, The lattice expansion of iron, in: Proc. R. Soc. London A Math. Phys. Eng. Sci., The Royal Society, 1955: pp. 459–467.
[39] E.H. Lee, P.J. Maziasz, A.F. Rowcliffe, J.R. Holland, L.K. Mansur, D.I. Potter, The structure and composition of phases occuring in austenitic stainless steels in thermal and irradiation environments, By JR Holland, LK Mansur DI Potter, AIME, New York. (1981) 191.
[40] Y. Matsukawa, T. Takeuchi, Y. Kakubo, T. Suzudo, H. Watanabe, H. Abe, T. Toyama, Y. Nagai, The two-step nucleation of G-phase in ferrite, Acta Mater. 116 (2016) 104–113.
[41] G. Rixecker, R. Haberkorn, Fe16Nb6Si7 and Fe16Ta6Si7: New D8a phases synthesized by the crystallization of mechanically alloyed amorphous powders, J. Alloys Compd. 316 (2001) 203–208.
[42] C.P. Wang, Y. Hu, S.Y. Yang, Y. Lu, Q.W. Jiang, X.J. Liu, Experimental investigation of phase equilibria in the Fe-Si-Zr ternary system, J. Phase Equilibria Diffus. 34 (2013) 277–288.
[43] D.J.M. King, Datasets relating to "G-phase strengthened iron alloys by design," (2019).
[44] A.E. Carlsson, P.J. Meschter, Relative stability of LI2, DO22, and DO23 structures in MAl3 compounds, J. Mater. Res. 4 (1989) 1060–1063.
[45] T.J. Chung, W.H. Moon, Y.G. Park, M.C. Kim, C.K. Choi, First-principle study on substitution of Cu or P into Ni–Sn intermetallic compounds, Intermetallics. 18 (2010) 1228–1234.
[46] J.M. Vitek, S.A. David, D.J. Alexander, J.R. Keiser, R.K. Nanstad, Low temperature aging behavior of type 308 stainless steel weld metal, Acta Metall. Mater. 39 (1991) 503–516.
[47] T. Yamada, S. Okano, H. Kuwano, Mechanical property and microstructural change by thermal aging of SCS14A cast duplex stainless steel, J. Nucl. Mater. 350 (2006) 47–55.
[48] H.M. Chung, T.R. Leax, Embrittlement of laboratory and reactor aged CF3, CF8, and CF8M duplex stainless steels, Mater. Sci. Technol. 6 (1990) 249–262.
[49] L. Byeong-Joo, L.D. Nyung, A thermodynamic study on the VC and Fe-V systems, Calphad. 15 (1991) 283–291.
[50] C. Pareige, J. Emo, S. Saillet, C. Domain, P. Pareige, Kinetics of G-phase precipitation and spinodal decomposition in very long aged ferrite of a Mo-free duplex stainless steel, J. Nucl. Mater. 465 (2015) 383–389.
[51] M. Miller, K. Russell, Embrittlement of RPV steels : An atom probe tomography perspective, J. Nucl. Mater. 371 (2007) 145–160.
[52] J.M. Hyde, G. Sha, E. a. Marquis, a. Morley, K.B. Wilford, T.J. Williams, A comparison of the structure of solute clusters formed during thermal ageing and irradiation, Ultramicroscopy. 111 (2011) 664–671.
[53] M.K. Miller, K.A. Powers, R.K. Nanstad, P. Efsing, Atom probe tomography characterizations of high nickel , low copper surveillance RPV welds irradiated to high fluences, J. Nucl. Mater. 437 (2013) 107–115.
[54] J.F. Knott, C.A. English, Views of TAGSI on the principles underlying the assessment of the mechanical

properties of irradiated ferritic steel Reactor Pressure Vessels, Int. J. Press. Vessel. Pip. 76 (1999) 891–908.
[55] P.D. Styman, J.M. Hyde, K. Wilford, A. Morley, G.D.W. Smith, Precipitation in long term thermally aged high copper, high nickel model RPV steel welds, Prog. Nucl. Energy. 57 (2012) 86–92.
[56] P.D. Styman, J.M. Hyde, K. Wilford, G.D.W. Smith, Quantitative methods for the APT analysis of thermally aged RPV steels, Ultramicroscopy. 132 (2013) 258–264.
[57] R.A. Mulford, jr McMahon CJ, D.P. Pope, H.C. Feng, Temper embrittlement of Ni-Cr steels by phosphorus, Metall. Trans. A. 7 (1976) 1183–1195.
[58] P.D. Styman, J.M. Hyde, D. Parfitt, K. Wilford, M.G. Burke, C.A. English, P. Efsing, Post-irradiation annealing of Ni–Mn–Si-enriched clusters in a neutron-irradiated RPV steel weld using Atom Probe Tomography, J. Nucl. Mater. 459 (2015) 127–134.
[59] C. Pareige, S. Novy, S. Saillet, P. Pareige, Study of phase transformation and mechanical properties evolution of duplex stainless steels after long term thermal ageing (> 20 years), J. Nucl. Mater. 411 (2011) 90–96.
[60] D.J.M. King, M.R. Wenman, Comment on “The two-step nucleation of G-phase in ferrite”, the authors: Y. Matsukawa et al. Acta Mater 2016; 116: 104–133, Scr. Mater. 163 (2019) 163–165.
[61] N. Almirall, P.B. Wells, T. Yamamoto, K. Wilford, T. Williams, N. Riddle, G.R. Odette, Precipitation and Hardening in Irradiated Low Alloy Steels with a Wide Range of Ni and Mn Compositions, Acta Mater. (2019).
[62] B. Jenkins, Improving the safety and reliability of reactor pressure vessel steels, (2019).
[63] F. González, Y. Houbaert, A review of ordering phenomena in iron-silicon alloys, Rev Met. 49 (2013) 178–199.
[64] K.H. Lo, C.H. Shek, J.K.L. Lai, Recent developments in stainless steels, Mater. Sci. Eng. R Reports. 65 (2009) 39–104.
[65] M. Kolenda, A. Szytuła, J. Leciejewicz, C. Maletka, Magnetic properties of Mn6Ni16Si7 and Mn3Cr3Ni16Si7, J. Magn. Magn. Mater. 96 (1991) 121–124.
[66] S.J. Ahmed, J.E. Greedan, C. Boyer, M. Niewczas, Magnetic and Structural Studies of G-Phase Compound Mn6Ni16Si7, Inorg. Chem. 57 (2018) 14144–14151.

APPENDIX

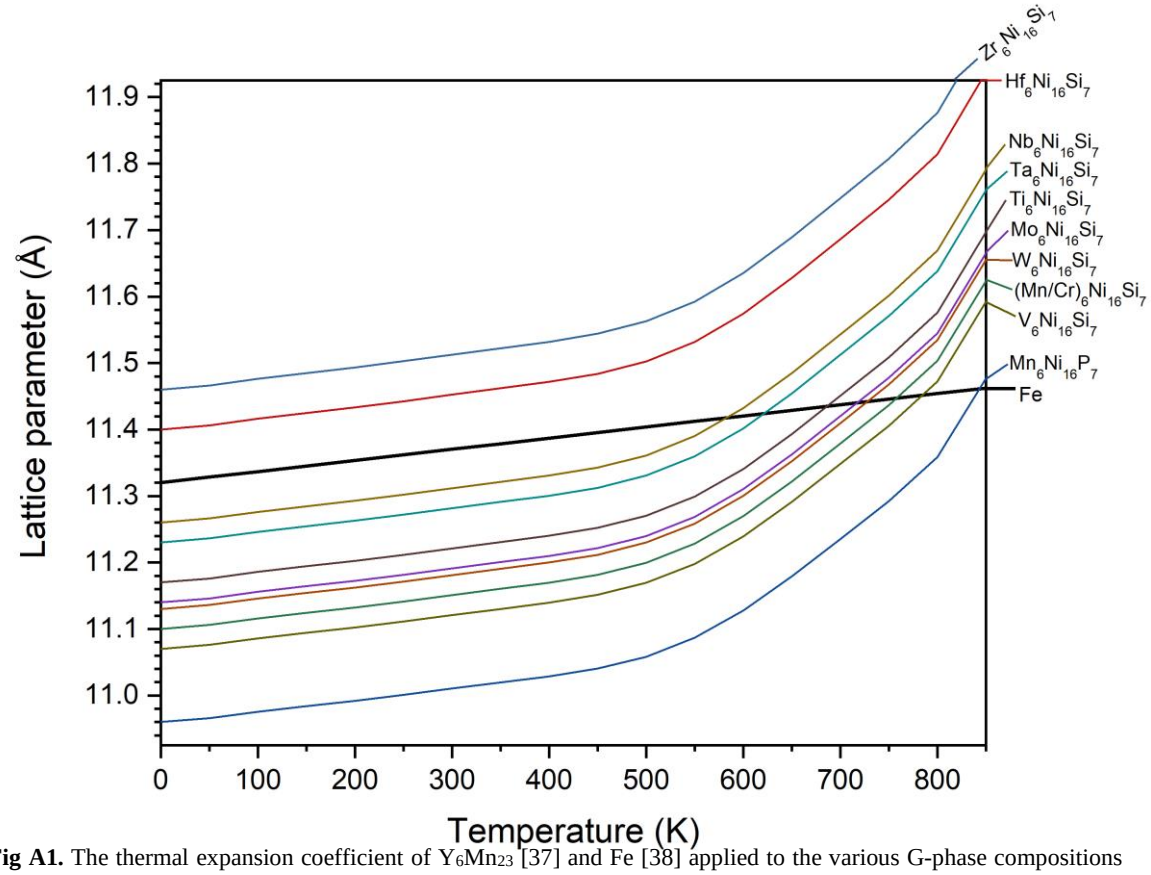


Fig A1. The thermal expansion coefficient of Y_6Mn_{23} [37] and Fe [38] applied to the various G-phase compositions and Fe lattice parameters calculated at 0 K in this study.

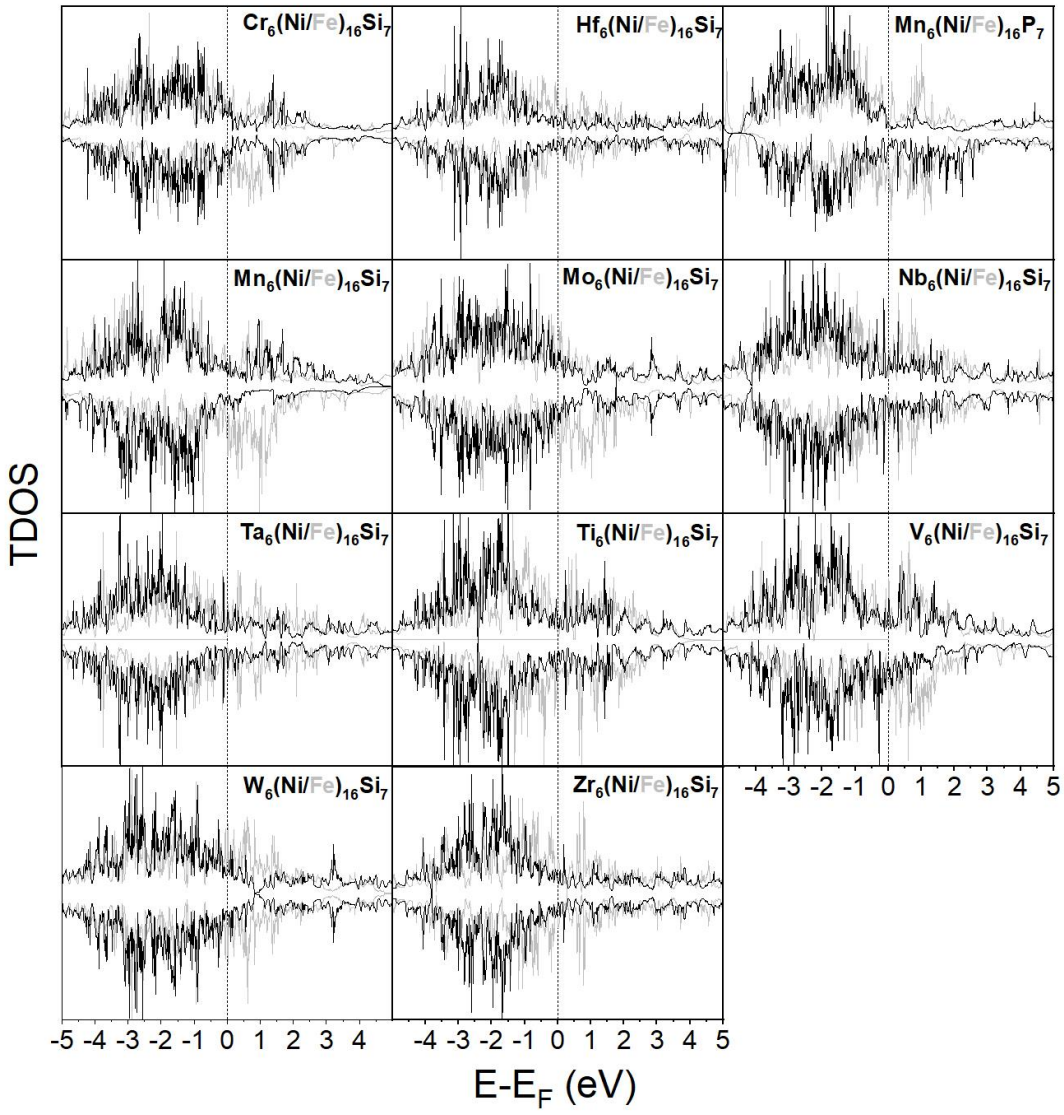


Fig A2. Total density of states (TDOS) of G-phase 29 atom unit cells where each panel corresponds the two labelled compositions containing Ni (solid dark line) and Fe (solid light line). The dashed vertical lines indicate the position of the Fermi level.

When comparing the TDOS of G-phases with the same X component, distinct differences in shapes are seen when X is Mn, Cr, Mo and V. This is due to the magnetic moments of each X component, predicted by DFT, observed as an anisotropy of the upper and lower spin channels of the TDOS, which is not seen in their non-magnetic counterparts. The magnetic moments were calculated are as follows:

- 3.5 μ_B for Mn, in $Mn_6Ni_{16}Si_7$, which is within the range measured by neutron diffraction (1.7 μ_B [65] – 4.7 μ_B [66]).
- 0.4 μ_B for Cr in $Cr_6Fe_{16}Si_7$.

- 0.1 μ_B for Mo in $Mo_6Fe_{16}Si_7$.
- 1.0 μ_B for V in $V_6Fe_{16}Si_7$, when in the presence of Fe;

It should be noted that the non-magnetic $Mn_6Ni_{16}Si_7$ structure was also simulated and found to have a 2.81 eV/unit less favourable formation enthalpy and lattice parameter 0.19 Å smaller than its magnetic counterpart.

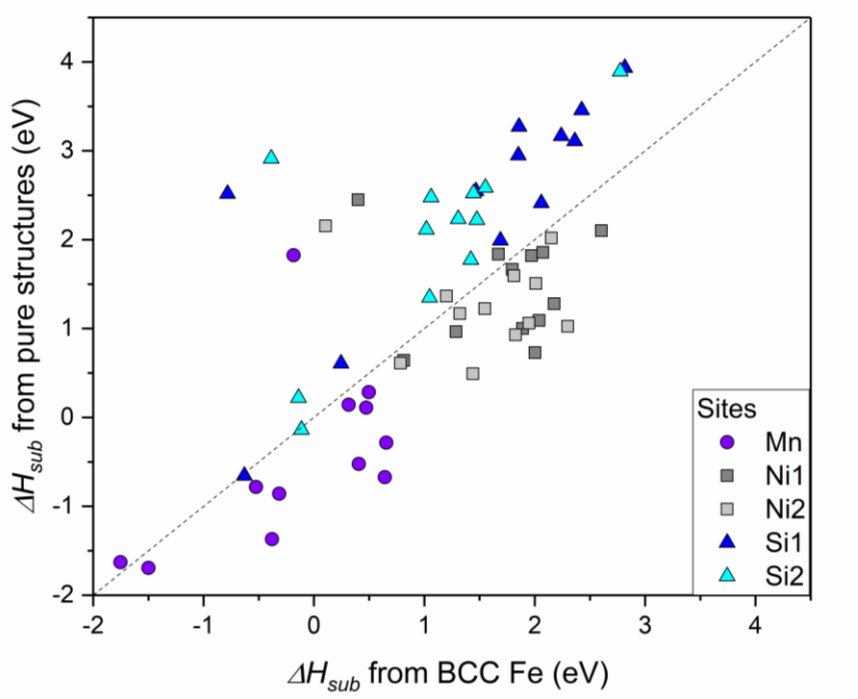


Fig A3. Comparison of conventional calculation of the substation energy (y-axis) to the method used within this study (x-axis) for Mn (circle), Ni (square), and Si (triangle) lattice sites of the G-phase.

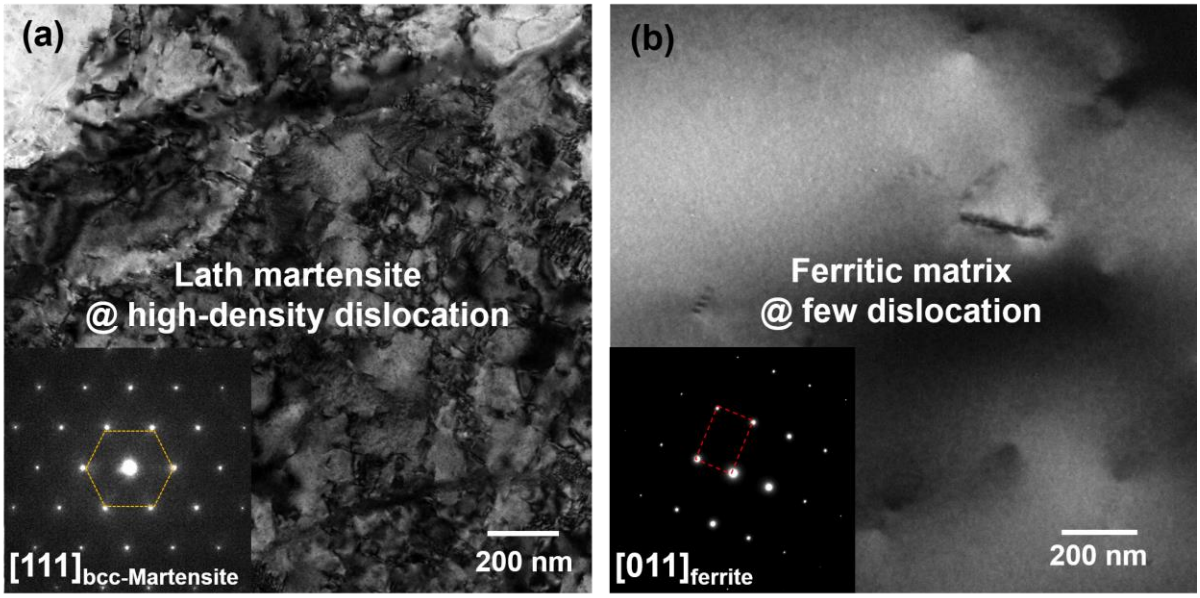


Fig A4. SAED patterns of comparison compositions (a) $Fe_{bal}Ni_7Si_2Mn_1$ and (b) $Fe_{bal}Ni_3Si_3Mn_1$.